



Emergence of chaos in magnetic-field-driven skyrmionsGyuyoung Park  and Sang-Koog Kim ^{*}*National Creative Research Initiative Center for Spin Dynamics and Spin-Wave Devices, Nanospinics Laboratory, Research Institute of Advanced Materials, Department of Materials Science and Engineering, Seoul National University, Seoul 08826, Republic of Korea*

(Received 19 August 2023; revised 1 November 2023; accepted 1 November 2023; published 28 November 2023)

We explore magnetic-field-driven chaos in magnetic skyrmions. Oscillating magnetic fields induce nonlinear dynamics in skyrmions, arising from the coupling of the secondary gyrotropic mode with a nonuniform, breathinglike mode. Through micromagnetic simulations, we observe complex patterns of hypotrochoidal motion in the orbital trajectories of the skyrmions, which are interpreted using bifurcation diagrams and local Lyapunov exponents. Our findings demonstrate that different nonlinear behaviors of skyrmions emerge at distinct temporal stages, depending on the nonlinear dynamic parameters. Investigating the abundant dynamic patterns of skyrmions during the emergence of chaos not only enhances device reliability but also provides useful guidelines for establishing chaos computing based on skyrmion dynamics.

DOI: [10.1103/PhysRevB.108.174441](https://doi.org/10.1103/PhysRevB.108.174441)**I. INTRODUCTION**

Chaos presents a fundamental phenomenon in nonlinear dynamics, observed in various systems, in both classical and quantum-mechanical oscillators. Nonlinear dynamical systems can exhibit diverse behaviors, including fixed points, periodic and quasiperiodic, and chaotic motions. This transition from the regular nonlinear behavior to chaos is a typical process on the quasiperiodic route to chaos. Importantly, these behaviors can manifest at different temporal stages within a single system [1]. For instance, a system may initially exhibit periodic motion before transitioning to chaos, or it may start with quasiperiodic motion and gradually become chaotic over time.

In the field of spintronics, topologically protected spin textures like skyrmions have garnered significant attention due to their potential applicability in low-power-driven high-density data storage [2,3], and ultrafast information processing, thanks to their topological stability at the nanoscales [4]. Therefore, delving into the nonlinearity within skyrmion dynamics and any potential chaotic effects is crucial for ensuring reliable device utilization. While chaotic dynamics of other topological spin textures, such as current-driven magnetic vortices [5,6] and antiferromagnetic bimerons [7], have been studied, reports on chaotic dynamics of skyrmions are relatively rare, even though their nonlinear dynamics have been examined in previous studies [8]. Further research is needed to fill this gap and explore chaotic dynamics in magnetic skyrmions.

In this paper, we begin by investigating the field-driven nonlinear dynamics of magnetic skyrmions, which exhibit complex hypotrochoidal trajectories. Subsequently, we map the various regimes of the skyrmion's nonlinear behavior over time, building a comprehensive nonlinear dynamic phase

map. This map illustrates the transition from regular to chaotic regime along temporal space versus the amplitude of the oscillating magnetic fields. Additionally, by exploring and harnessing the chaotic behavior of skyrmions, we may pave the way for applications in chaos-based computing and signal processing. Therefore, our findings provide valuable insights for designing future skyrmion-based technologies with enhanced functionalities and reliability.

II. METHODS

The model employed in the present study involves a Néel-type skyrmion formed in a circular nanodisk with a radius (R_{disk}) of 30 nm and a thickness of 0.6 nm, as shown in its ground state in Fig. 1(a). To reduce the magnetostatic energy at the boundary of the disk, spins at the edge are tilted toward the center of the skyrmion. To numerically calculate the dynamic motion of the skyrmion, we used the MUMAX3 code [9], which utilizes the Landau-Lifshitz-Gilbert (LLG) equation: $\partial\mathbf{M}/\partial t = -\gamma\mathbf{M} \times \mathbf{H}_{\text{eff}} + (\alpha_G/M_s)\mathbf{M} \times \partial\mathbf{M}/\partial t$, where γ is the gyromagnetic ratio, α_G is the Gilbert damping constant, and \mathbf{H}_{eff} is the effective field given as $\mathbf{H}_{\text{eff}} = -(1/\mu_0)\partial E_{\text{tot}}/\partial\mathbf{M}$. The total energy, E_{tot} , includes the magnetostatic, magnetocrystalline anisotropy, exchange, and intrinsic Dzyaloshinskii-Moriya interaction (DMI), and Zeeman energies. The Dormand-Prince (RK-45) method was used to solve the LLG equation with a maximum error per step set to 10^{-5} . This level of precision reliably facilitated the study and characterization of the nonlinear and chaotic behaviors inherent in the spin system. For the material, we assumed Co interfaced with Pt and used the following parameters: perpendicular anisotropic constant $K_u = 4 \times 10^5$ J/m³, exchange constant $A_{\text{ex}} = 1.5 \times 10^{11}$ J/m, interfacial DMI constant $D_{\text{int}} = 3$ mJ/m², Gilbert damping constant $\alpha_G = 0.01$, and saturation magnetization $M_s = 0.58 \times 10^6$ A/m. A cell size was set to $0.6 \times 0.6 \times 0.6$ nm³.

^{*}Corresponding author: sangkoog@snu.ac.kr

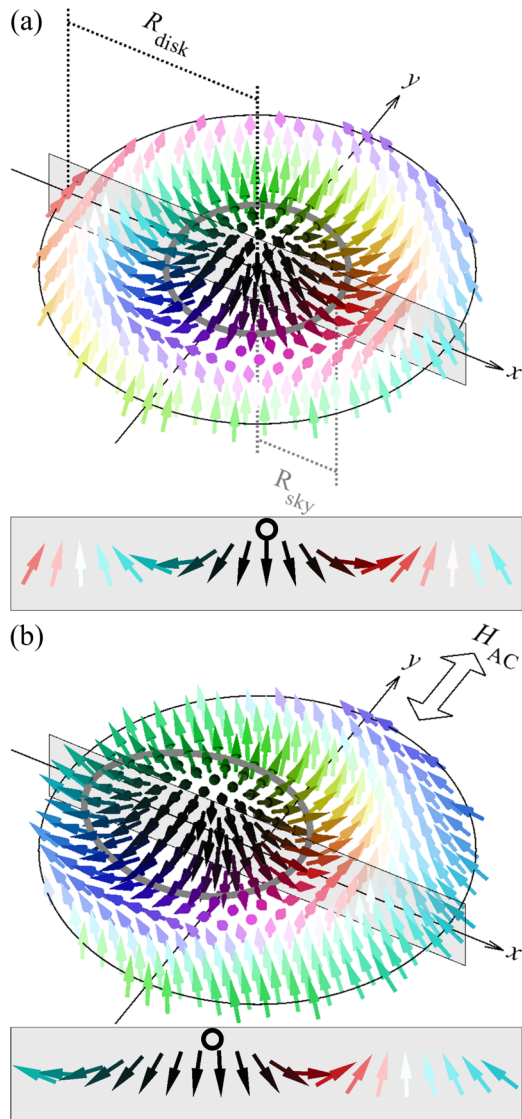


FIG. 1. (a) Ground-state magnetization ($\mathbf{m} = \mathbf{M}/M_S$) configuration of a Néel-type skyrmion confined within a nanodisk. (b) A snapshot of the magnetization configuration of the same skyrmion at an arbitrary moment during excitation by a sinusoidal magnetic field (H_{AC}) applied along the y axis. The domain wall of the skyrmion is represented by the gray circle shown in each spin configuration. Insets show spin profiles of the gray-shaded boxes. The positions of the guiding center in each state are indicated by the black wide circles.

With the aforementioned conditions, we intentionally formed the Néel-type skyrmion with a core polarization of -1 (spin down) and allowed it to relax to reach its ground state. In the ground state, the skyrmion exhibits a circular domain wall represented by the gray circle, indicating a radius (R_{sky}) [10] of about 12.5 nm. We applied a linearly polarized harmonic field, $H_{AC} = A \sin(2\pi f_+ t)$, uniformly over the entire disk along the y axis. The field amplitude A can be expressed as $\alpha = A/A_s$ [11] and A_s ($=2730$ Oe) represents a static field used to annihilate the skyrmion. We gradually increased α from 0 to 0.30 in increments of 5×10^{-4} . By considering the skyrmion's iner-

tial mass \mathcal{M} [12], Thiele's equation of motion is [13]

$$-\mathcal{M}\ddot{\mathbf{R}} + G \times \dot{\mathbf{R}} - K\mathbf{R} = 0. \quad (1)$$

We obtained the angular frequencies of two gyrotropic modes as follows:

$$w_{\pm} = -G/2\mathcal{M} \pm \sqrt{(G/2\mathcal{M})^2 + (K/\mathcal{M})}. \quad (2)$$

The higher or secondary gyrotropic mode, denoted as f_+ ($f_+ = w_+/2\pi \approx 21.37$ GHz; cf. $f_- \approx 2.19$ GHz at zero external field), represents a counterclockwise rotation in this core polarity of spin down. Here, G is the gyrocoupling constant, K is the spring constant, and $\mathbf{R} = (X, Y)$ represents the guiding center with $X = \int x q dx dy / \int q dx dy$ and $Y = \int y q dx dy / \int q dx dy$, where $q = (1/4\pi)\mathbf{m} \cdot (\partial_x \mathbf{m} \times \partial_y \mathbf{m})$ is the topological charge density [14].

Unlike the lower or fundamental gyrotropic mode, where the entire skyrmion moves as a rigid body, the higher gyrotropic mode exhibits nonlinear behavior (see Supplemental Material [8,15]). In the f_+ mode, the core and peripheral spins gyrate in the same direction, but in out of phase when the skyrmion is excited [16]. This leads to a coupling between the in-plane gyrotropic mode and a nonuniform out-of-plane breathinglike [17] mode. Consequently, during the application of a driving force, the skyrmion undergoes a deformation that breaks its rotational symmetry. When the topological soliton experiences deformation, its moment of inertia and spring constant are altered, giving rise to the soliton's nonlinear dynamics [18,19]. This deformation-induced nonlinear dynamics exclusively occurs when the skyrmion is driven by the higher gyrotropic mode. In Fig. 1(b), we illustrated the deformed skyrmion during its gyration. The gray circle shows the distorted contour of the skyrmion's domain wall, which assumes an irregular ellipselike shape due to the broken rotational symmetry of the breathinglike mode being coupled with its gyration mode. A profile of the individual spins' orientations across the center is shown below the skyrmion illustration. Compared to the ground state, the number of black spins inside the skyrmion's domain wall increases from five to seven. Small black circles just above the black spins denote the position of the guiding center at that moment. The guiding center follows an orbital motion during the gyration, resembling a hypotrochoid, which belongs to the family of curves known as roulettes.

III. RESULTS

The hypotrochoid is traced by a point attached to a circle with radius b , rolling inside a fixed circle with radius a , where the point is a distance d from the interior circle's center. The general hypotrochoid can be represented by the complex parametrization:

$$z(t) = r_1 e^{i w_1 t} + r_2 e^{-i w_2 t}, \quad (3)$$

where the geometric parameters are related as follows: $d = r_2$, $b = (w_1/w_2)r_1$, and $a = [(w_1 + w_2)/w_2]r_1$. When the higher gyrotropic mode is excited, the orbital motion represented by the guiding center inevitably follows one of the hypotrochoids [12,19]. The Thiele's equation [Eq. (1)] can be modified with the linearly polarized oscillating magnetic field as

$$-\mathcal{M}\ddot{\mathbf{R}} + G \times \dot{\mathbf{R}} - K\mathbf{R} + \mu(\dot{\mathbf{z}} \times \mathbf{H}) = 0, \quad (4)$$

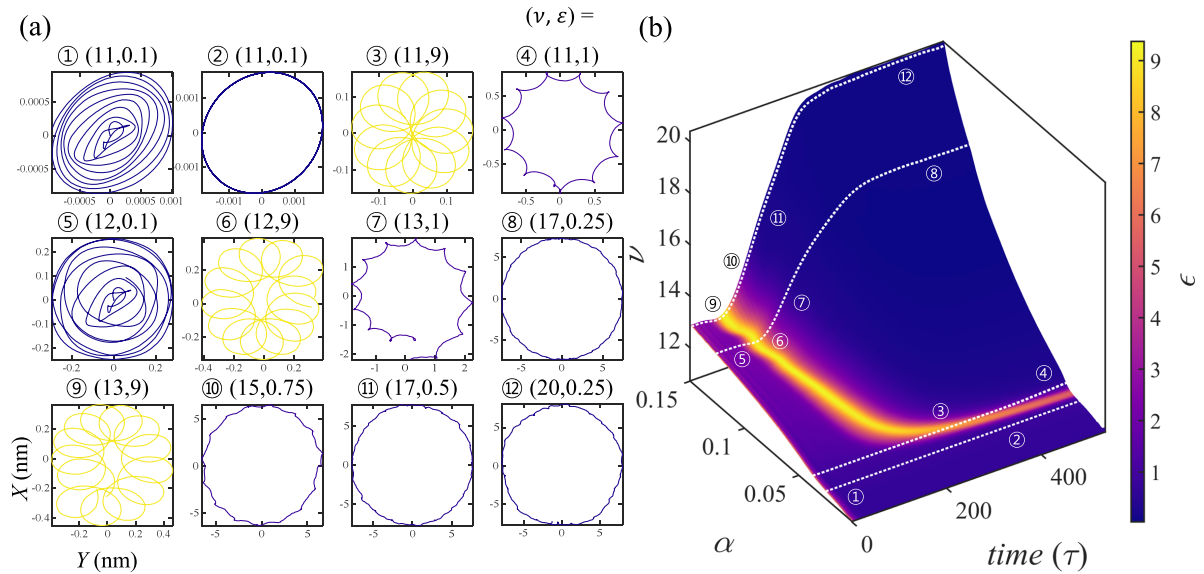


FIG. 2. (a) Orbital trajectories of skyrmion motions calculated using the guiding center over the time interval of $t_i \sim t_i + 1/f_-$ at indicated values of (ν, ε) (refer to labels ① through ⑫). (b) Calculations of ν and ε plotted on the plane of evolution time versus field amplitude, α . The values of ε are indicated by the color scheme in the color bar to the right. White dotted lines represent constant α values of 0.0245, 0.0365, 0.126, and 0.1485.

with $\mathbf{H} = (0, \alpha A_s \sin(w_+ t), 0)$, and the solution of Eq. (4) is

$$R(t) = r_- e^{iw_- t} + \left(r_+ + \frac{h}{2} \right) e^{iw_+ t} - \frac{h}{2} e^{-iw_+ t} \quad (5)$$

with $h = \mu \alpha A_s \sin^2 w_+ t / (\mathcal{M} w_+^2 + K)$. Equation (5) takes a form similar to that of the hypotrochoids, Eq. (3). Note that the two gyrotropic modes w_{\pm} have opposite signs, indicating the opposite rotation sense. Since $R(0) = 0$, $r_- = -r_+ = (-w_- + w_+)h/w_+$. Therefore, the hypotrochoidal parameters for the skyrmion are given as $r_1 = (-w_- + w_+)h/w_+$ and $r_2 = (r_+ + \frac{h}{2}) = (2w_- - w_+)h/2w_+$. So far, the equation of motion has been linear. However, it becomes nonlinear as the eigenfrequencies, denoted by Eq. (2), vary during the motion. Due to the skyrmion's deformation under oscillation causes changes in \mathcal{M} and K , where $\mathcal{M} = \zeta \bar{r}$ and $K = \xi \bar{r}^2$ [20], with ζ and ξ being deformation-induced coefficients, and r representing the local radial distance of the closed domain wall. Furthermore, r varies significantly for irregularly shaped skyrmions [21].

The shape of the hypotrochoid can be defined by two parameters, namely, the number of cusps, $\nu = a/b = (w_1 + w_2)/w_1$, and the ratio of the distance to the smaller radius, $\varepsilon = d/b = r_2 w_2 / r_1 w_1$. The value of ε determines the type of the hypotrochoid. For example, in either case of $(w_1 > w_2$ and $\varepsilon < 1$) or $(w_1 < w_2$ and $\varepsilon > 1$), the curve is a prolate hypotrochoid. Conversely, if the opposite conditions are met, the curve is a curtate hypotrochoid. When $\varepsilon = 1$, the curve is a hypocycloid.

Figure 2(a) illustrates the representative shapes of the orbital trajectories for the indicated values of (ν, ε) , which are also labeled by ① – ⑫ in Fig. 2(b) for four different values of α (i.e., $\alpha = 0.0245, 0.0365, 0.126$, and 0.1485). These α values fall within distinct transition spaces between different nonlinear behaviors. The parameter ν was estimated from the

fast Fourier transform of the trajectories over time, while ε was derived from a geometrical analysis of $\mathbf{R}(X, Y)$ without any fitting. The number of cusps in each orbital geometry corresponds well with each ν value. Meanwhile, when $\varepsilon = 1$, the hypotrochoid becomes a hypocycloid, as seen in cases ④ and ⑦. In this skyrmion system, $w_1 (=|w_-|)$ is always smaller than $w_2 (=|w_+|)$. Therefore, trajectories with $\varepsilon > 1$ exhibit prolate hypotrochoids, as observed in cases ③, ⑥, and ⑨, while trajectories with $\varepsilon < 1$ display curtate hypotrochoids, as in cases ⑧, ⑩, ⑪, and ⑫.

Figure 2(b) depicts the hypotrochoidal parameters of ν and ε as functions of evolution time and reduced field amplitude α (0–0.15) for skyrmion motions excited by oscillating magnetic fields. It is important to note that beyond $\alpha = 0.157$, the skyrmion breaks down [18,22,23] within the observation time from 0 to 534τ , where τ represents one period of the modulation frequency and is equivalent to the inverse of the frequency of the higher gyrotropic mode, $1/f_+$. In the plots of (ν, ε) , two distinct navy regions are separated by the maximum ε values (yellow line) along given α values. For t and α below the yellow line, the skyrmion motions show fixed points or periodic motions, while they exhibit quasiperiodic and chaotic motion on the condition above the yellow line. Furthermore, a transition is observed from a prolate-type to a curtate-type configuration beyond the line of maximum ε .

Next, we turn our attention to various nonlinear regimes related to the nonlinear parameters. Analyzing a single variable, such as the orbital radius $\rho = |\mathbf{R}|/R_{\text{sky}}$, offers a highly effective method to classify different types of nonlinear behaviors depending on the nonlinear parameters. In our analysis, we identified six critical points: $\alpha = 0.0245$ for the shift from a fixed point to periodic motion; $\alpha = 0.0365$ for the transition from periodic to quasiperiodic motion; $\alpha = 0.126$ and $\alpha = 0.1485$ for the gradual transitions to complex quasiperiodicities; $\alpha = 0.152$ for the transition from quasiperiodic motion

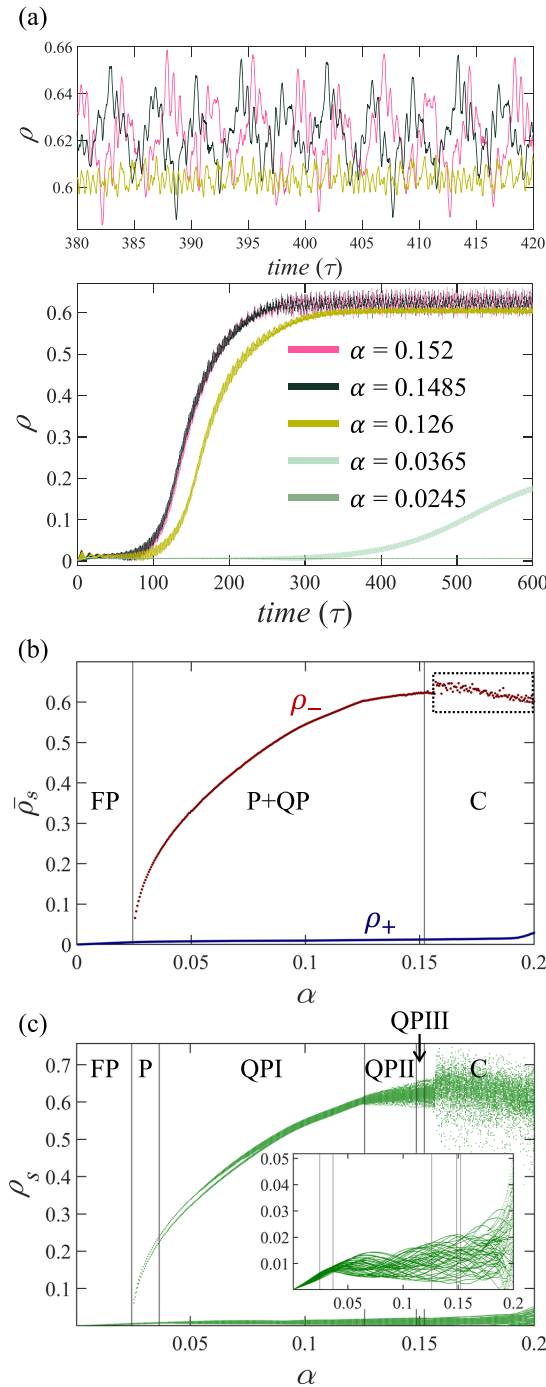


FIG. 3. (a) The orbital radius, ρ , versus time for selected field amplitudes ($\alpha = 0.0245, 0.0365, 0.126, 0.1485$, and 0.152). The upper panel shows the steady states of ρ for 380τ to 420τ for $\alpha = 0.126, 0.1485$, and 0.152 . (b) The two steady states, ρ_{\pm} , as functions of α . The labels F, P, QP, and C symbolize the regimes of distinct nonlinear behaviors: fixed point, periodic, quasiperiodic, and chaotic motion, respectively. (c) The bifurcation diagram of ρ_s as a function of α with an inset showing an enlarged view of the region where $\rho_s \leq 0.05$.

to chaos; and finally, at $\alpha = 0.1565$, the skyrmion begins to break down during its motion.

For a more qualitative analysis of the nonlinear behaviors, we plotted ρ as a function of time for $\alpha = 0.0245, 0.0365$,

$0.126, 0.1485$, and 0.152 , as illustrated in Fig. 3(a). When the skyrmion is driven by the higher gyrotropic mode, ρ exhibits two steady states, ρ_{\pm} , at different temporal stages: an initial unstable ρ_+ state, followed by a later stable ρ_- state. In the ρ_+ state, the skyrmion is underdamped, while in the ρ_- state, it becomes overdamped due to the changes in K . For $\alpha < 0.0245$, the skyrmion does not reach the ρ_- state, hindered by an energy barrier that primarily originates from the damping force. This regime is a fixed point where the guiding center asymptotically approaches the ρ_+ state after extensive gyration. As α surpasses 0.0245 , ρ increases, and its steady state, ρ_s , oscillates around the ρ_- state. As α continues to increase, the transition from ρ_+ to ρ_- becomes more rapid. Specifically, at $\alpha = 0.0365$, the ρ_- state is achieved after a few hundred periods of oscillation. In this regime of $\alpha < 0.0365$, ρ exhibits a periodic behavior in its steady states, whereas it becomes quasiperiodic (or loosely periodic) for $\alpha \geq 0.0365$. In this latter regime, some variations in the signal do not conform to regular periodicities. For $\alpha = 0.126$ and $\alpha = 0.1485$, the quasiperiodicities gradually become much more complex. Finally, at $\alpha = 0.152$, regular periodicities start to diminish, and chaos begins to occur. The signals shown at the top of Fig. 3(a) for $\alpha = 0.126, 0.1485$, and 0.152 allow us to better visualize these periodicities. Unlike the cases of $\alpha = 0.126$ and 0.1485 , the case of $\alpha = 0.152$ has no periodicities, indicating a transition from quasiperiodic to chaotic motions. When $\alpha \geq 0.152$, a well-known property of chaos, the sensitive dependence on initial conditions (SDI), arises. For these values of α , signals with minor differences in initial conditions can result in substantial variations in the resulting signals.

Figure 3(b) displays the two steady states, ρ_{\pm} , against α . The separate ρ_{\pm} values were identified with $\langle \rho_s \rangle$ values. The different nonlinear regimes are labeled as fixed points (FP), periodic (P), and quasiperiodic (QP) motion, and chaos (C). The chaotic regime was differentiated by the concept of SDI. With SDI, even an extremely small variance in the initial conditions can lead to vastly different outcomes. In the breakdown regime, indicated by black dotted boxes for $\alpha \geq 0.1565$, ρ_{\pm} exhibit large variations. This distribution signifies that even an extremely small difference in initial conditions, such as $\Delta q < 10^{-5}$, can significantly alter the lifetime of the skyrmion within this regime (see Supplemental Material [23]). Furthermore, the ρ_- value generally decreases in the breakdown regime, indicative of high instability in the dynamics of the skyrmion.

A bifurcation diagram can facilitate a comprehensive understanding of potential long-term behaviors and highlight different periodicities that arise with changes in a key bifurcation parameter. In this context, ρ_s represents the long-term periodic behavior, while α acts as the bifurcation parameter. For example, Fig. 3(c) presents the bifurcation diagram of ρ_s versus α , offering a visual guide to the field-driven skyrmion's quasiperiodic route to chaos. The diagram outlines different stages, previously detailed in Fig. 3(b), and marks each bifurcation point with black vertical lines. As α increases, both ρ_- and ρ_+ bifurcate, but the skyrmion does not oscillate between the ρ_{\pm} states, back and forth. The inset figure highlights the ρ_+ states. Unlike the FP regime, ρ_s increases progressively in the P region. Through a series of bifurcations in the QP regime,

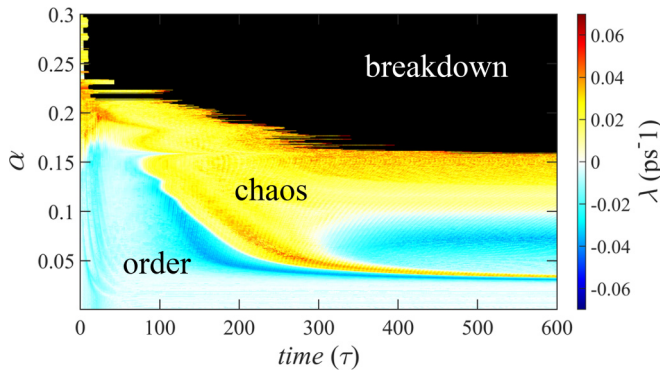


FIG. 4. Estimation of the local Lyapunov exponent as a function of time and field amplitude, α , with the color bar representing the value of $\lambda(t)$ at each point.

specifically denoted as QPI, QPII, and QPIII—distinguished by the amount of information in the steady states—the nonlinear dynamics of the skyrmion transition into the chaos regime. Here, ρ_s can take on every possible value, as evidenced by the scattered data points. This result effectively describes the series of quasiperiodic routes to chaos.

Finally, we estimated the local Lyapunov exponent, denoted as $\lambda(t)$, a measure of sensitivity to initial conditions in a dynamical system, evaluated locally in the phase space (i.e., over a short period of time at a specific point). We constructed the $\lambda(t)$ map from the time trace of the speed, v , of the guiding center $\mathbf{R}(X, Y)$ as follows [24]:

$$\lambda(t) = \frac{\delta(t + \Delta t) - \delta(t)}{\Delta t} \quad (6)$$

and

$$\delta(t) = \frac{1}{N} \sum_{i=1}^N \ln \left(\frac{\|\vec{V}_{i+t} - \vec{V}_{i^*+t}\|}{\|\vec{V}_i - \vec{V}_{i^*}\|} \right), \quad (7)$$

where $\vec{V}_i = [v_i, v_{i+\tau}]$ is the reconstructed phase space with time delay τ and \vec{V}_{i^*} is the nearest neighbor such that $\|\vec{V}_i - \vec{V}_{i^*}\|$ is minimized. In the resultant $\lambda(t)$ map, with respect to α and t , as shown in Fig. 4, blue regions (where $\lambda < 0$) depict the exponential convergence of trajectories in the phase space, representing stable ordered states. In contrast, red regions (where $\lambda > 0$) indicate the exponential divergence of trajectories in the phase space, signifying chaotic states or ordered but unstable expanding states. White regions (where $\lambda \approx 0$), situated between the red and blue regions, represent a transition space between order and chaos, known as the edge of chaos. A black region at the top of the map denotes the breakdown regime.

The previously classified regimes of nonlinear dynamics in the bifurcation map match well with the $\lambda(t)$ map at $t \approx 0$. However, the $\lambda(t)$ map strongly suggests that the nonlinear behavior changes over time, as evidenced in the map of hy-

potrochoidal parameters. Furthermore, the maximum ε line shown in Fig. 2 coincides with the narrow white line observed on the left side of Fig. 4, which is an initial transition zone from order to chaos, i.e., the edge of chaos. This line indicates a transition from stable to unstable states (for $\alpha < 0.152$) or from ordered to chaotic states (for $\alpha \geq 0.152$). For $0 < \alpha < 0.0365$, the skyrmion maintains its ordered state throughout the oscillation. For $0.0365 \leq \alpha < 0.1$, it begins with a stable limit cycle or torus and displays intermittent unstable ordered states due to repelling trajectories between ρ_+ and ρ_- states. For $0.1 \leq \alpha < 0.15$, the skyrmion's dynamic states shift from stable state to unstable. For $0.15 \leq \alpha < 0.17$, the skyrmion shows transient chaos in the initial states. For $0.17 \leq \alpha$, the skyrmion displays chaotic dynamics throughout the oscillation until it breaks down.

IV. CONCLUSION

We investigated the nonlinear dynamic behaviors of a magnetic skyrmion driven by oscillating magnetic fields. The nonlinear mode arises from the coupling of gyrotropic modes with a nonuniform breathinglike mode. The deformation of the skyrmion altered key properties such as its moment of inertia and spring constant, which in turn affected the eigenfrequency of the fundamental gyrotropic mode. This led to changes in the characteristic parameters, including the cusp number and the type of hypotrochoid, leading to the complex hypotrochoidal motions of the skyrmion over time. By constructing a bifurcation map and a local Lyapunov exponent map, we were able to distinguish the entire range of nonlinear behaviors, spanning from ordered regimes to chaos, across various field amplitudes and temporal stages. This in-depth understanding of the field-strength and time-dependent chaotic dynamics of magnetic skyrmions provides essential insights into its quasiperiodic route to chaos. Furthermore, it can foster the development of innovative computation schemes [25,26] that leverage the initial condition-sensitive, deterministic chaos dynamics. For example, within the chaotic regime, the dynamics of the skyrmion markedly differ based on its initial condition. One can categorize the initial conditions that exhibit similar dynamic patterns into specific logic functions. This approach enables a single skyrmion to function as a reprogrammable logic gate capable of executing a wide range of logic operations.

ACKNOWLEDGMENTS

This research was supported by the Basic Science Research Program through the National Research Foundation of Korea (NRF), funded by the Ministry of Science and ICT, South Korea (Grant No. 2021R1A2C2013543) and Samsung Electronics Co., Ltd. (Grant No. IO201229-08274-01). The Institute of Engineering Research at Seoul National University provided additional research facilities for this work.

- [1] M. Shapiro and G. Goelman, Onset of chaos in an isolated energy eigenstate, *Phys. Rev. Lett.* **53**, 1714 (1984).
- [2] N. Romming, C. Hanneken, M. Menzel, J. E. Bickel, B. Wolter, K. von Bergmann, A. Kubetzka, and R. Wiesendanger,

Writing and deleting single magnetic skyrmions, *Science* **341**, 636 (2013).

- [3] S. S. P. Parkin, M. Hayashi, and L. Thomas, Magnetic domain-wall racetrack memory, *Science* **320**, 190 (2008).

- [4] F. Jonietz, S. Mühlbauer, C. Pfleiderer, A. Neubauer, W. Münzer, A. Bauer, T. Adams, R. Georgii, P. Böni, R. A. Duine, K. Everschor, M. Garst, and A. Rosch, Spin transfer torques in MnSi at ultralow current densities, *Science* **330**, 1648 (2010).
- [5] T. Devolder, D. Rontani, S. Petit-Watelot, K. Bouzehouane, S. Andrieu, J. Létang, M.-W. Yoo, J.-P. Adam, C. Chappert, S. Girod, V. Cros, M. Sciamanna, and J.-V. Kim, Chaos in magnetic nanocontact vortex oscillators, *Phys. Rev. Lett.* **123**, 147701 (2019).
- [6] S. Petit-Watelot, J.-V. Kim, A. Ruotolo, R. M. Otxoa, K. Bouzehouane, J. Grollier, A. Vansteenkiste, B. Van de Wiele, V. Cros, and T. Devolder, Commensurability and chaos in magnetic vortex oscillations, *Nat. Phys.* **8**, 682 (2012).
- [7] L. Shen, J. Xia, X. Zhang, M. Ezawa, O. A. Tretiakov, X. Liu, G. Zhao, and Y. Zhou, Current-induced dynamics and chaos of antiferromagnetic bimerons, *Phys. Rev. Lett.* **124**, 037202 (2020).
- [8] Y.-f. Chen, Z.-x. Li, Z.-w. Zhou, Q.-l. Xia, Y.-z. Nie, and G.-h. Guo, Nonlinear gyrotropic motion of skyrmion in a magnetic nanodisk, *J. Magn. Magn. Mater.* **458**, 123 (2018).
- [9] A. Vansteenkiste, J. Leliaert, M. Dvornik, M. Helsen, F. Garcia-Sanchez, and B. Van Waeyenberge, The design and verification of MuMax3, *AIP Adv.* **4**, 107133 (2014).
- [10] X. S. Wang, H. Y. Yuan, and X. R. Wang, A theory on skyrmion size, *Commun. Phys.* **1**, 31 (2018).
- [11] K.-S. Lee and S.-K. Kim, Gyrotropic linear and nonlinear motions of a magnetic vortex in soft magnetic nanodots, *Appl. Phys. Lett.* **91**, 132511 (2007).
- [12] I. Makhfudz, B. Krüger, and O. Tchernyshyov, Inertia and chiral edge modes of a skyrmion magnetic bubble, *Phys. Rev. Lett.* **109**, 217201 (2012).
- [13] A. A. Thiele, Steady-state motion of magnetic domains, *Phys. Rev. Lett.* **30**, 230 (1973).
- [14] N. Papanicolaou and T. N. Tomaras, Dynamics of magnetic vortices, *Nucl. Phys. B* **360**, 425 (1991).
- [15] M. Mruczkiewicz, P. Gruszecki, M. Krawczyk, and K. Y. Guslienko, Azimuthal spin-wave excitations in magnetic nanodots over the soliton background: Vortex, Bloch, and Néel-like skyrmions, *Phys. Rev. B* **97**, 064418 (2018).
- [16] C. Moutafis, S. Komineas, and J. A. C. Bland, Dynamics and switching processes for magnetic bubbles in nanoelements, *Phys. Rev. B* **79**, 224429 (2009).
- [17] S.-Z. Lin, C. D. Batista, and A. Saxena, Internal modes of a skyrmion in the ferromagnetic state of chiral magnets, *Phys. Rev. B* **89**, 024415 (2014).
- [18] Z. Chen, X. Zhang, Y. Zhou, and Q. Shao, Skyrmion dynamics in the presence of deformation, *Phys. Rev. Appl.* **17**, L011002 (2022).
- [19] M.-W. Yoo, F. Mineo, and J.-V. Kim, Analytical model of the deformation-induced inertial dynamics of a magnetic vortex, *J. Appl. Phys.* **129**, 053903 (2021).
- [20] K.-W. Moon, B. S. Chun, W. Kim, Z. Q. Qiu, and C. Hwang, Control of skyrmion magnetic bubble gyration, *Phys. Rev. B* **89**, 064413 (2014).
- [21] D. R. Rodrigues, A. Abanov, J. Sinova, and K. Everschor-Sitte, Effective description of domain wall strings, *Phys. Rev. B* **97**, 134414 (2018).
- [22] L. Liu, W. Chen, and Y. Zheng, Current-driven skyrmion motion beyond linear regime: Interplay between skyrmion transport and deformation, *Phys. Rev. Appl.* **14**, 024077 (2020).
- [23] See Supplemental Material at <http://link.aps.org/supplemental/10.1103/PhysRevB.108.174441> for details on the (non)linear characteristics of the skyrmions in-plane excitations, as well as the breakdown and the SDI associated with the nonlinear mode.
- [24] M. T. Rosenstein, J. J. Collins, and C. J. De Luca, A practical method for calculating largest Lyapunov exponents from small data sets, *Physica D (Amsterdam, Neth.)* **65**, 117 (1993).
- [25] S. Sinha and W. L. Ditto, Dynamics based computation, *Phys. Rev. Lett.* **81**, 2156 (1998).
- [26] S. Sinha and W. L. Ditto, Computing with distributed chaos, *Phys. Rev. E* **60**, 363 (1999).